Frequency conversion interposer with no-internal stress curved-beam for MEMS vibrational energy harvesters

Ueno, Hidetaka
Toshiyoshi, Hiroshi
Suzuki, Takaaki

(Citation)
Sensors and Actuators A: Physical,378:115750

(Issue Date)
2024-11-01

(Resource Type)
journal article

(Version)
Version of Record

Sensors & Actuators: A. Physical 378 (2024) 115750

Contents lists available at ScienceDirect

Sensors and Actuators: A. Physical

journal homepage: www.journals.elsevier.com/sensors-and-actuators-a-physical

Frequency conversion interposer with no-internal stress curved-beam for MEMS vibrational energy harvesters

Hidetaka Ueno [a,b,c,*], Hiroshi Toshiyoshi [d], Takaaki Suzuki [e,**]

[a] Center for Advanced Medical Engineering Research & Development (CAMED), Kobe University, 1-5-1 Minatojima-minamimachi, Chuo-ku, Kobe, Hyogo 650-0047, Japan
[b] Department of Medical Device Engineering, Graduate School of Medicine, Kobe University, 7-5-1 Kusunoki-cho, Chuo-ku, Kobe, Hyogo 650-0017, Japan
[c] Health and Medical Research Institute, National Institute of Advanced Industrial Science and Technology (AIST), 2217-14 Hayashi-cho, Takamatsu, Kagawa 761-0395, Japan
[d] Institute of Industrial Science (IIS), The University of Tokyo, 4-6-1 Komaba, Meguro-ku, Tokyo 153-8505, Japan
[e] Division of Mechanical Science and Technology, Gunma University, Kiryu, Gunma 376-8515, Japan

ARTICLE INFO

Keywords:
Energy harvesting
Vibration energy harvester
MEMS
Interposer
Bistable
Frequency conversion

ABSTRACT

The generating efficiency of an micro electro mechanical system vibrational energy harvester (MEMS VEH), which converts vibrational energy into electrical energy, is maximized at resonance. However, because the resonance frequency of an MEMS VEH is an order of magnitude higher than the vibrational frequency in the environment and not only has a high Q value, but the frequency of vibration in the environment changes randomly, it is difficult for MEMS VEHs to harvest vibrational energy efficiently. In this study, we propose a method to improve the generation efficiency of MEMS VEHs using a Frequency Conversion Interposer (FCI) that vibrates nonlinearly with its bistable no-internal stress curved-beam. As a simulation model combining FCI with the MEMS VEH, we fabricated a Two-Dimensional Monolithic Structure (TDMS) with a curved-beam and a straight beam that mimicked the FCI and oscillatory structure of the MEMS VEH, respectively. It was observed that the vibration of the straight beam induced snap-through (ST) of the curved-beam of the FCI, and the measured acceleration was more than 1.3 times the applied acceleration applied from the FCI to the MEMS VEH. As the power generation of the MEMS VEH is proportional to the square of the applied acceleration, the FCI is useful for improving the generating efficiency of the MEMS VEH.

1. Introduction

Wireless Sensor Networks (WSN) are being constructed to realize an Internet of Things (IoT) society that shares, analyzes, and feeds back all information in the living environment, making society safe and efficient [1–3]. WSNs are constructed using wireless sensors on the order of trillions [4]. Because many wireless sensors must function as sensor nodes independent of the power source, a small power source (battery) must be mounted on the wireless sensor. However, conventional rechargeable or replaceable power sources (batteries) have low durability and high replacement costs, making them difficult to use as sensor node power sources that require long-term autonomous operation.

Energy Harvesters (EH) that directly retrieve energy from the environment and convert it into electrical energy have been developed with the aim of applying them to batteries mounted on sensor nodes [5]. The general power sources for EH are light [6], heat [7], electromagnetic waves [8], and vibrations [9]. Photovoltaic power, such as solar power, is widely used as a renewable energy source. Although the energy density of sunlight is up to 15 mW/cm^3, there are significant restrictions on the usage environment such as weather and location [10]. In addition, there are problems with the use environment and low energy density for thermal energy harvesters that generate power owing to temperature differences and electromagnetic wave power generation that generates power owing to communication waves. However, vibration occurs in various environments where the use of sensor nodes is assumed, such as the human body, home appliances, buildings, and industrial equipment, and is less affected by weather; thus, the vibration power generation method has high versatility compared to other power

* Correspondence to: Therapeutic Medical Device Development Division, Center for Advanced Medical Engineering Research & Development (CAMED), Kobe University, 1-5-1 Minatojima-minamimachi, Chuo-ku, Kobe, Hyogo 650-0047, Japan.
** Correspondence to: Division of Mechanical Science and Technology, Gunma University, 1-5-1 Tenjin-cho, Kiryu, Gunma 376-8515, Japan.
E-mail addresses: hueno@people.kobe-u.ac.jp (H. Ueno), suzuki.taka@gunma-u.ac.jp (T. Suzuki).

https://doi.org/10.1016/j.sna.2024.115750
Received 20 May 2024; Received in revised form 14 July 2024; Accepted 26 July 2024
Available online 27 July 2024
0924-4247/

generation methods. In addition, its vibrational energy density is higher than that of other energy sources in the environment [11]. Therefore, Vibration Energy Harvesters (VEH) with advantages in versatility and energy density are actively being conducted [12,13]. VEH, which generates power by vibrating an oscillatory structure with a mass point, includes piezoelectric type that generates power by the piezoelectric effect that occurs when a piezoelectric body deforms and distorts [14], electromagnetic induction type that generates power by the change in electric field caused by the relative motion of a magnet and coil [15,16], friction type that generates power by the charge movement caused by the difference in charge column when two materials are contacted [17], electrostatic induction type that generates power by the charge movement associated with the change in electrostatic capacity due to the change in the gap of opposing electrodes [18], and various power generation methods such as hybrid type that combines multiple mechanisms [19,20]. In recent years, it has been developed using semiconductor/microelectromechanical systems (MEMS) fabrication technology, which is excellent for miniaturization, integration, and mass production. VEHs manufactured with these technologies are called MEMS VEH [21–23]. Microelectromechanical systems (MEMS) VEH, which are easy to miniaturize, enhance functions, and reduce costs/high throughput compared to other VEHs, are gaining attention as power sources for integration on sensor nodes. The generating efficiency of the MEMS VEH is maximized at the resonance of the oscillatory structure, and the generating efficiency without resonance is one-tenth that at resonance; therefore, to improve the generating efficiency of the MEMS VEH, the natural frequency of the oscillatory structure is adjusted according to the input frequency [24,25]. However, even when various methods are used, the resonance frequency of the MEMS VEH is still an order of magnitude higher than the vibrational frequency in the environment. Additionally, it has a high Q value, and efficient energy conversion using resonance phenomena is difficult. Furthermore, because the frequency of vibrations in the environment changes randomly, it is extremely difficult for existing MEMS VEH to efficiently convert the vibrational energy in the environment.

Generally, it is expected that the generation efficiency of the MEMS VEH can be improved by integrating a bistable structure that vibrates nonlinearly to the interposer, connecting the MEMS VEH and the circuit board, and converting random vibrations in the environment [26]. The vibration of a bistable structure with two stable equilibrium positions exhibits intrawell oscillations that do not involve movement between stable equilibrium positions, chaotic vibrations that involve movement between stable equilibrium positions called snap-through (ST) that vibrate nonlinearly, and interwell oscillations that vibrate linearly between stable equilibrium positions [27]. In particular, in chaotic vibrations and interwell oscillations, impulse vibrations due to ST, which involve changes in stable equilibrium positions, occur continuously. Because ST occurs due to the potential energy possessed by the bistable structure, the magnitude of the acceleration resulting from ST does not correlate with the acceleration and frequency of the applied vibrations from the environment. By applying a bistable structure to the interposer that connects the MEMS VEH and circuit board and converts random vibrations in the environment into impulse vibrations, it is expected that various environmental vibrations can be converted and efficiently supplied to MEMS VEH without being affected by the frequency of the applied vibrations. A bistable structure is mainly constructed by assembling small magnets and spring structures with internal stress [28–31]. However, an interposer structure constructed by combining multiple elements, such as magnets and springs, is not suitable for batch fabrication, assembly, and packaging processes using semiconductor/MEMS processing technology, and there are challenges in the miniaturization and mass production required for sensor node power sources.

In this study, we propose a method to improve the generation efficiency of existing MEMS VEH by combining a Frequency Conversion Interposer (FCI) with a bistable structure and a no-internal stress curved-beam. The proposed FCI only has planar and no-internal stress curved-beams. Thus, they can be fabricated and packaged using existing semiconductor/MEMS processing technology, making them suitable for miniaturization and mass production of sensor nodes [32–35]. In this study, we demonstrate the usefulness of the proposed FCI for improving the generating efficiency of MEMS VEH using a two-dimensional monolithic structure (TDMS) with a curved-beam of FCI and a simulated oscillatory structure of a MEMS VEH. Specifically, we fabricated a TDMS with a curved-beam of FCI and a simulated oscillatory structure of a MEMS VEH and evaluated the acceleration conversion function of the FCI. First, we analyzed the bistable characteristics depending on the shape of the curved-beam of the TDMS by elucidating the force-displacement curve (F-D curve) using the finite element method (FEM). Next, we fabricated the TDMS, which is a two-dimensional planar structure, by machining in one direction. Finally, when the vibration was applied to the fabricated TDMS, the acceleration of the converted vibration applied to the mimicking part of the MEMS VEH was measured using a no-internal stress curved-beam. By comparing the applied acceleration from the environment and the acceleration converted by the FCI, which determines the electrical power generated by the MEMS VEH, we evaluated the acceleration conversion function of the FCI. The definition of abbreviations is shown in Table 1.

2. FCI evaluation using TDMS

The power generation device that combines the FCI with a no-internal stress curved-beam, which is a bistable structure, and the MEMS VEH with an oscillatory structure is a two-freedom vibration degree system with two vibration parts. In this study, we applied periodic vibrations to the TDMS that modeled this combined power generation device and evaluated the vibration conversion function of the no-internal stress curved-beam of the FCI. Interposers are used in various electronic devices to connect electronic components such as semiconductors and circuit boards. A normal interposer is a no-deformable substrate integrated with an electrical circuit using a microfabrication process normally used for fabricating semiconductors [36]. In the proposed method, by using the FCI, which is an interposer with a deformable no-internal stress curved-beam, the acceleration of ST due to the nonlinear vibration of the FCI induced by vibrations from the environment is applied to the MEMS VEH without significantly deviating the device manufacturing/packaging process and device size from the general size. Additionally, by making the FCI shape that can be manufactured in one direction, it is possible to mass-produce and integrate it with electrodes using semiconductor processing technology, similar to a regular interposer.

In the power generation mechanism of the power generation device composed of the MEMS VEH and FCI, first, the vibration input from the environment induces the ST of the no-internal stress curved-beam of the bistable structure of the FCI, and the acceleration due to the ST is applied to the MEMS VEH. Next, the oscillatory structure of the MEMS VEH generates electrical power by vibrating owing to the ST. Fig. 1 shows a schematic of the TDMS, which is a model that combines the MEMS VEH and FCI. The MEMS VEH has a mass point (Mass), oscillatory structure, and connection parts (electrical and mechanical connection points) that transmit electric energy to other parts. The FCI has an electrode that

Table 1
Definition of abbreviations in this paper.

Abbreviation	Definition
VEH	Vibration energy harvester
FCI	Frequency conversion interposer
TDMS	Two-dimensional monolithic structure
ST	Snap-through
F-D curve	Force-displacement curve
FEM	Finite element method

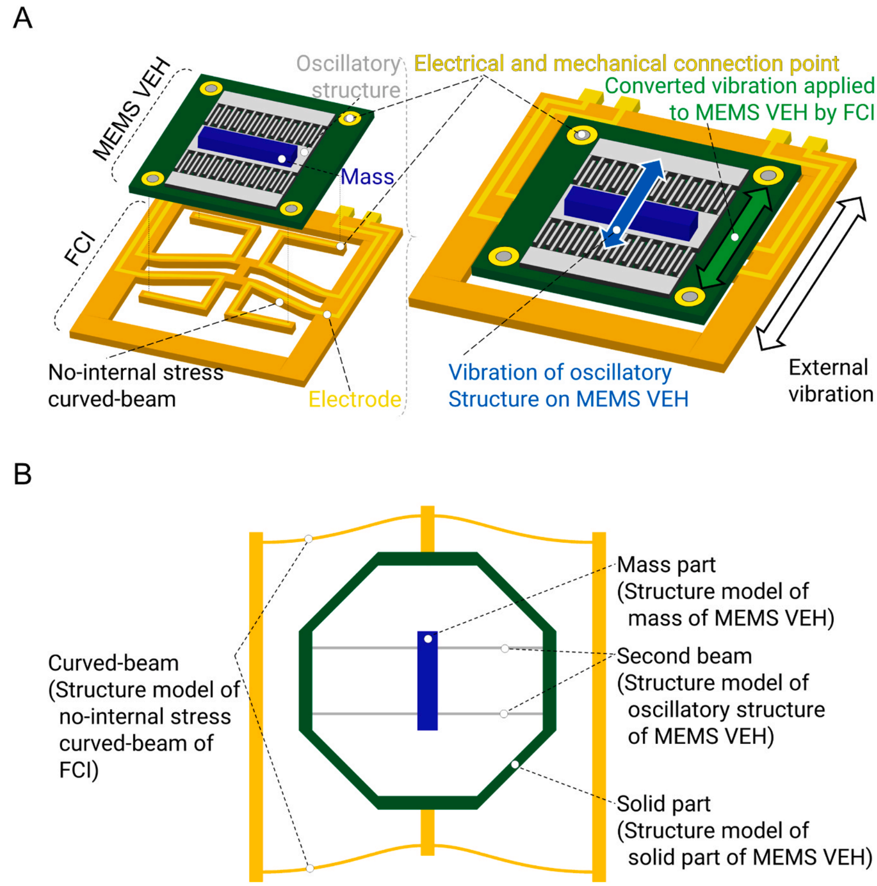

Fig. 1. Conceptual image of TDMS for simulating the FCI assembled to MEMS VEHs with an oscillatory structure. (A) Schematic image of energy harvesting system composed of FCI and MEMS VEH. (B) Schematic image of TDMS that is a model of FCI assembled to MEMS VEHs.

receives electrical energy from the MEMS VEH and transmits it to other parts and a no-internal stress curved-beam that converts vibrations from the outside to nonlinear vibrations. The MEMS VEH and FCI were connected at the electrical and mechanical connection points, as indicated by yellow circles. The applied external vibration, including the impulse vibration (white arrow in Fig. 1(A)), is converted in both magnitude and period by the ST of the no-internal stress curved-beam of the FCI (green arrow in Fig. 1(A)). The converted vibration generated the vibration of the mass point of the MEMS VEH and electrical power (blue arrow in Fig. 1(A)). The ST of the no-internal stress curve-beam causes large displacements and accelerations, and its magnitude does not correlate with the vibration frequency of the vibration from the environment. Therefore, it is expected that the FCI with a no-internal stress curved-beam can efficiently supply vibration energy in the environment, which is a wideband random vibration, to the MEMS VEH regardless of its frequency. Because the vibrations indicated in green and blue mutually influence each other through a complex mechanism, we created a verification model to directly demonstrate and evaluate the vibration phenomena. The verification model TDMS used in this study has a mass part that mimics the oscillatory structure with the mass point (Mass) of the MEMS VEH, a solid part that is the nondriving part of the MEMS VEH, and a curved-beam that mimics the no-internal stress curved-beam of the FCI (Fig. 1(B)). The acceleration characteristics of the converted vibration applied from the FCI to the MEMS VEH were clarified by measuring the vibration of the solid part of the TDMS when the vibration was applied from the outside to the TDMS with a laser displacement sensor. Through these verifications, the effectiveness of the FCI on the power generation efficiency of the MEMS VEH was evaluated.

3. Structural mechanics analysis

The Finite Element Method (FEM) was used to evaluate the vibrational characteristics of TDMS. The FEM was performed using computer aided engineering software (COMSOL, Inc.; COMSOL Multiphysics 5.4) to verify the bistability of the TDMS. The designed shape and material properties of the TDMS are illustrated in Fig. 2. The TDMS has two oscillatory structures: a curved-beam with an initial displacement H and a second beam, which is a parallel beam, within an approximately 50 mm square (Fig. 2(A)). The curved-beam had a thin film hinge, the length of which is shown I (Fig. 2(B)). In addition, the initial displacement of the curved-beam is H. The value of I was designed in 4 mm increments from 0 to 8 mm, and H was designed in 2 mm increments from 0 to 4 mm. Each model is described using the values of I and H. For example, a model with a thin film hinge part length I of 4 and an initial displacement H of 2 is described as I4H2. The material properties of polycarbonate, which is a TDMS material, are shown in Fig. 2(C). In the analysis, both sides of the TDMS model were fixed, and the reaction force of the TDMS was calculated from the applied force when a predetermined displacement was made at the tip of the TDMS. A F-D curve was also plotted. In the F-D curve, the displacement and reaction force are on the horizontal and vertical axes, respectively. The F-D curve of a typical bistable structure is shown in Fig. 3. The F-D curve of a typical bistable structure has six characteristic values. The maximum reaction force and its displacement against deformation are f_{top} and d_{top}, respectively. When the reaction force is zero, it is d_{mid}. The maximum values of the reaction force that occurred in the same direction as the deformation and displacement were f_{bot} and d_{bot}, respectively. The displacement when the reaction force becomes zero after further deformation is d_{end}. The bistable structure generates a reaction force in

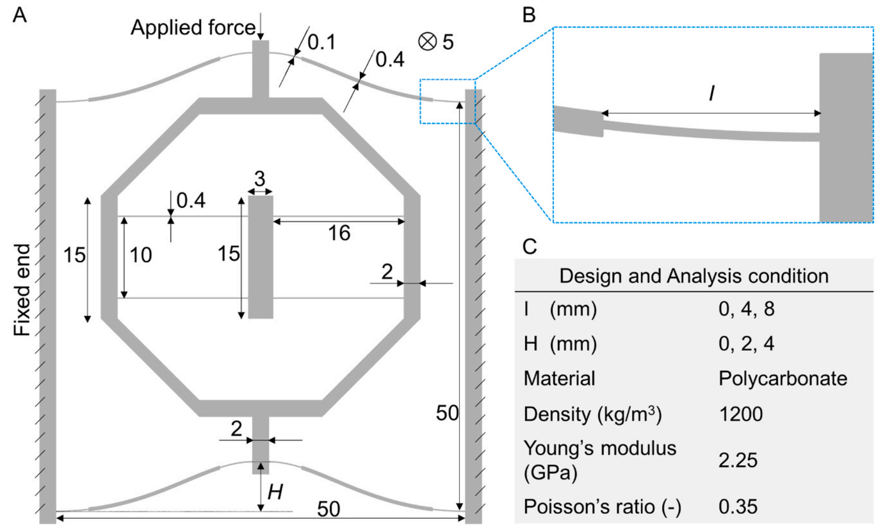

Fig. 2. Analytical model of TDMS. (A) Overall of analytical model of TDMS. The unit in the figure is millimeter. (B) Enlarged image of thin film hinge. (C) Other analysis conditions.

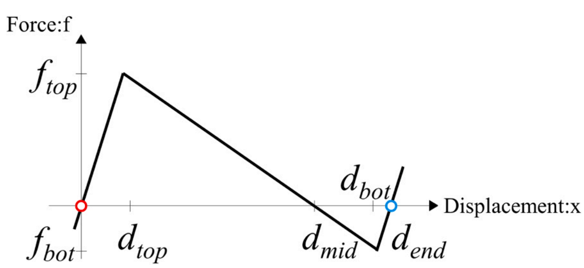

Fig. 3. Typical F-D curve of a bistable, pre-shaped curved-beam. Red and blue circles mean the first and second stable equilibrium points, respectively.

the direction opposite to that of deformation. As shown in Fig. 3, the direction of the reaction force is positive.

The characteristics of the bistable structure were evaluated based on the shape of the F-D curve. The minimum energy E_1, required to move from the first stable equilibrium point, which is the first stable equilibrium point, to the opposite second stable equilibrium point, is represented by Eq. (1).

$$E_1 = \int_0^{d_{mid}} f(x)dx \tag{1}$$

Furthermore, the minimum energy required to move from the second stable equilibrium point to the first stable equilibrium point E_2 is given by Eq. (2).

$$E_2 = -\int_{d_{mid}}^{d_{end}} f(x)dx \tag{2}$$

The smaller the absolute values of E_1 and E_2, the smaller is the input energy required to cause a shift in the stable position. The ratio R of the magnitudes of E_1 and E_2 is represented by Eq. (3).

$$R = \frac{E_2}{E_1} \tag{3}$$

The difference in energy between the directions of the ST was smaller and correlated to R. This means that the smaller R is, the more stable the ST that can be generated under sinusoidal vibration.

The FEM analysis was performed using nine TDMS analysis models with different I and H, and the F-D curves for each model were plotted. The F-D curves for each model are shown in Fig. 4. Graphs with maximum transverse force values of 2.0 N and 0.25 N are shown in Fig. 4(A) and Fig. 4(B), respectively. For models with an initial displacement H of 0 mm, the reaction force increased with the displacement, and the F-D curve was not N-shaped. The F-D curve of I0H2 was N-shaped, but f_{bot} was not negative. The reaction forces of the other models followed an N-shaped F-D curve, and f_{bot} exhibited a negative value. The characteristic values of the F-D curves for each model are listed in Table 2. Models I0H0, I4H0, and I8H0, which did not have an initial displacement, did not have an N-shaped F-D curve; therefore, the characteristic values on the F-D curve were not written. The reaction force of I0H2 was N-shaped; however, because f_{bot} is not negative, the values of d_{mid} and d_{end} were not described. The reaction

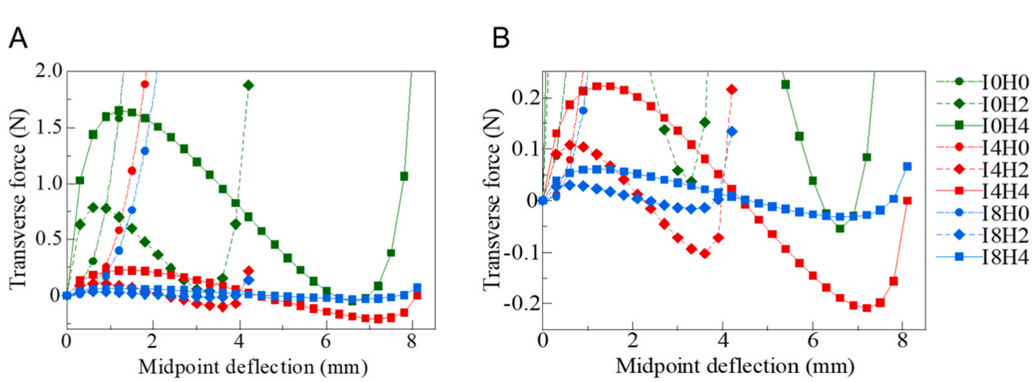

Fig. 4. Reaction forces calculated by FEM analysis. (A) Vertical scale is −0.25–2.0 N. (B) Vertical scale is −0.25–0.25 N.

Table 2
Calculated results of FEM analysis.

Model	f_{top} (N)	d_{top} (mm)	d_{mid} (mm)	-f_{bot} (N)	d_{bot} (mm)	d_{end} (mm)	$E_1 = \int_0^{d_{mid}} f(x)dx$ (mJ)	$E_2 = -\int_{d_{mid}}^{d_{end}} f(x)dx$ (mJ)	$1 - \frac{E_2}{E_1}$ (-)
I0H0	-	-	-	-	-	-	-	-	-
I0H2	(7.94×10^{-1})	(7.00×10^{-1})	-	($-3.45\times10-2$)	(3.20)	-	-	-	-
I0H4	1.65	1.30	6.20	5.43×10^{-2}	6.60	7.00	5.94	3.09×10^{-2}	9.95×10^{-1}
I4H0	-	-	-	-	-	-	-	-	-
I4H2	1.08×10^{-1}	7.00×10^{-1}	2.20	1.02×10^{-1}	3.60	4.00	1.57×10^{-1}	1.17×10^{-1}	2.55×10^{-1}
I4H4	2.23×10^{-1}	1.30	4.40	2.08×10^{-1}	7.20	8.10	6.44×10^{-1}	4.84×10^{-1}	2.48×10^{-1}
I8H0	-	-	-	-	-	-	-	-	-
I8H2	3.07×10^{-2}	6.00×10^{-1}	2.30	1.61×10^{-2}	3.40	3.90	4.40×10^{-2}	1.65×10^{-2}	6.25×10^{-1}
I8H4	6.12×10^{-2}	1.20	4.60	3.21×10^{-2}	6.70	7.80	1.75×10^{-1}	6.69×10^{-2}	6.18×10^{-1}

forces of I0H4, I4H2, I4H4, I8H2, and I8H4 had an N-shaped F-D curve, and f_{bot} had a negative value; therefore, all the characteristic values were described. In all the models that drew an N-shaped F-D curve containing a negative reaction force, E_1 was larger than E_2. In addition, the larger the length of the thin film hinge and the smaller the initial displacement, the smaller both E_1 and E_2 become. The value of R decreased in the following order: I4H4, I4H2, I8H4, I8H2, and I0H4. Models with an initial displacement H value of 0 mm all increased the reaction force with displacement, and because neither a negative reaction force nor an N-shaped F-D curve was observed, they were not bistable structures. In addition, the I0H2 model exhibited an N-shaped F-D curve; however, because f_{bot} is not a negative value and does not have a second stable position, it is not a bistable structure. However, for the other models, because the reaction force shows an N-shaped F-D curve and f_{bot} has a negative value, they are bistable structures. Therefore, it is indicated that multiple structures, either monostable or bistable, can be designed by only changing the size of the thin film hinge part and the initial displacement. However, because the energy ratio R required to move between stable positions was the smallest in the I4H4 model, it is also indicated that I4H4 has the smallest asymmetry with respect to the direction of the input vibration acceleration among the models.

4. Materials and methods

4.1. Fabrication of TDMS

The nine types of TDMS analyzed were fabricated by milling a polycarbonate plate in one direction. The fabricated shape is shown in Fig. 5. A structure for preventing lateral deformation and fixing it to the excitation shaker, shown in blue in the figure, was added to the TDMS analysis model shape, which included the curved-beam and the second beam shown in gray in the figure. The TDMS was fabricated using a 5 mm thick polycarbonate plate (PC 1600, TAKIRON Corporation) as the material and a numerical control (NC) milling machine (MDX-40A, Roland DG Corporation) with a 2 mm diameter end mill. To prevent structural damage and machining heat, the amount of machining per layer was set to 0.05 mm. Because the 5 mm thick polycarbonate plate was milled in one direction, no elastic or thermal deformation occurred in the polycarbonate plate during the milling process. Therefore, no internal stress was generated in the TDMS, which included the fabricated curved-beam and the second beam.

4.2. Vibrational experiment

Using feedback control with an accelerometer attached to the stage of the excitation shaker, we clarified the output acceleration of the primary beam of the TDMS when the stage of the excitation shaker vibrated sinusoidally with a constant maximum vibration acceleration amplitude by measuring the displacement of the solid part of the TDMS. The primary beam indicates a no-internal stress curved-beam and a non-curved-beam with an initial displacement H of 0 mm. The average acceleration of the TDMS was calculated by taking the second derivative of

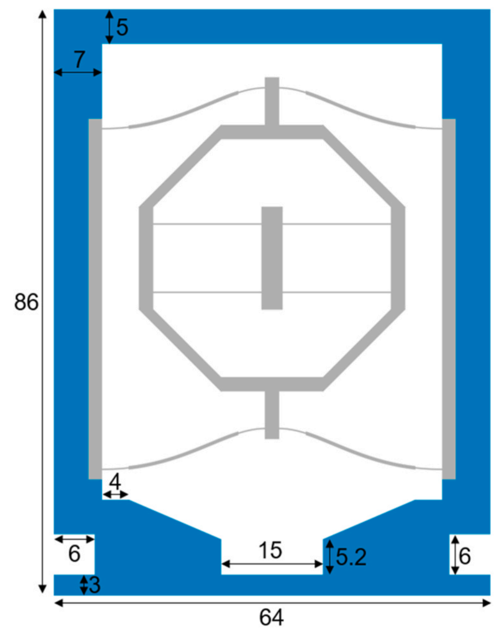

Fig. 5. Schematic image of TDMS fabricated by milling processing. The Gray area is the same shape as FEM analytical model. The Blue area is for fixing to excitation shaker and preventing the deformation of TDMS, except for the deformation of beams. The unit in the figure is a millimeter.

the displacement of the solid part using the central difference method. The acceleration that occurs in the primary beam of the TDMS can be directly measured by assembling a small accelerometer on the primary beam. However, there are concerns about the unexpected effect of the wire connecting the accelerometer. In this study, to measure the relationship between the applied acceleration and the output acceleration that changes owing to the interaction of two vibrating beams in a two-DOF vibration system, we obtained the average acceleration by measuring the displacement with a laser displacement sensor that did not impose physical constraints on the TDMS. In addition, the acceleration generated by the TDMS is due to nonlinear vibration, so it cannot be evaluated using the maximum acceleration, such as the linear vibration of a constant period. Therefore, regardless of the linearity or nonlinearity, we evaluated the relationship between the input acceleration of the TDMS and the output acceleration of the primary beam of the TDMS using the average acceleration, which is the average value of the acceleration of the vibration that occurs within a certain time.

Because the maximum acceleration amplitude achieved through feedback control using an accelerometer attached to the excitation shaker differs in principle from the average acceleration of the TDMS, it is not possible to make a direct comparison. Therefore, similar to the calculation of the average acceleration of the primary beam of the TDMS, the average acceleration applied to the TDMS from the excitation shaker was calculated by considering the second derivative of the displacement of the stage of the excitation shaker. The acceleration conversion function of the FCI was evaluated by directly comparing the average accelerations of the stage of the excitation shaker and TDMS primary beam, both of which were calculated using the second derivative with the central difference method. Specifically, the displacement of the stage of the excitation shaker was measured using a laser displacement meter when the excitation acceleration amplitude was varied in increments of 2.5 m/s^2 from 1 m/s^2 to 50 m/s^2. The vibration frequency was 10 Hz. The measurement time for the displacement during vibration was set to 20 s. The measured displacement was taken as the second derivative using the central difference method to calculate the acceleration applied to the TDMS at the excitation stage. Furthermore, the validity of the average acceleration obtained from the second derivative using the central difference method was evaluated by comparing the calculated average acceleration derived from the measured displacement of the stage with that derived from the maximum excitation acceleration amplitude.

To evaluate the acceleration generated in the solid part of the TDMS when subjected to vibrations, the TDMS and a laser displacement sensor were assembled on the stage of the excitation shaker, and the displacement of the solid part of the TDMS was measured using the laser displacement sensor. A schematic of the experimental vibration system is presented in Fig. 6. The TDMS and laser displacement sensors (LK-H080, KEYENCE CORPORATION) were placed on the stage of an excitation shaker (m060/MA1, IMV Corporation). During the vibration of the excitation shaker, the TDMS and laser displacement sensor, fixed on the same stage, vibrated at the same amplitude and frequency, allowing only the vibration of the primary beams with no internal stress from the TDMS to be detected. The laser emitted from the laser displacement sensor was reflected at the measurement point on a 2 mm thick polystyrene chip attached to the solid part of the TDMS. The oscillatory waveform converted by the primary beam was measured using the reflected laser light. During the vibration experiment, a 10.5 g weight was assembled to the mass part at the center of the TDMS. To clarify the effect of the vibration of the oscillatory structure of the MEMS VEH on the vibration of the FCI, vibration experiments were conducted under two conditions: with and without vibration of the mass of the TDMS using sinusoidal excitation. To suppress the vibration of the mass, the mass part and solid part of TDMS were fixed using an almost massless adhesive tape, normally called scotch tape. Vibration was applied to the TDMS via sinusoidal excitation. The frequency of the sinusoidal excitation was fixed at 10 Hz, which corresponded to a relatively low frequency of vibrations in the environment [37]. The measurement duration for the displacement during vibration was set to 20 s. Through feedback control using an accelerometer attached to the stage of the excitation shaker, the maximum value of the excitation acceleration amplitude during sinusoidal excitation was varied in increments of 2.5 m/s^2 from 1 m/s^2 to 50 m/s^2. The displacement of the solid part of the TDMS was measured, and the acceleration generated in the solid part was calculated by taking the second derivative using the central difference method.

5. Results and discussions

5.1. Fabrication of TDMS

The fabricated TDMS was evaluated using images taken by a scanning electron microscope (SEM, JCM-5700LV, JEOL Ltd.). The fabricated TDMS is shown in Fig. 7. By visual observation, there are no significant thickness variations in the milling direction or surface cracks observed in the fabricated TDMS (Fig. 7(A)). Even in the thinnest part of the thin film hinge, no significant cracks were observed (Fig. 7(B)). The fabricated values of the no-internal stress curved-beam with a design thickness of 400 μm and 100 μm were approximately 318 μm and 80 μm, respectively, and the thickness of the no-internal stress curved-beam was fabricated thinner than the design value. When cutting with an end mill, the end mill becomes larger than its original diameter owing to the adhesion of the adhesive used for the stage fixation of the polycarbonate plate. In addition, the cutting radius becomes larger than the diameter of the end mill owing to the offset of the rotation center axis of the end mill. These causes increased the machining amount more than the design value, and it is considered that the width of the no-internal stress curved-beam became smaller than the design value. In addition, during fabrication, no surface finishing or rough cutting, which is usually performed during cutting, was performed, and the cutting amount in the thickness direction was extremely small at 0.05 mm compared to general machining conditions, so it is considered that no significant damage such as cracks where stress concentrates occurred in TDMS. In addition, polycarbonate has a relatively high melting point compared to other resin materials such as polystyrene; therefore, it is considered that no internal stress occurred due to deformation caused by heat during cutting [38]. Therefore, although the film was thinner than the design value, a vibration experiment was conducted by modeling a secondary vibration system formed from the MEMS VEH and FCI using TDMS with a curved-beam without internal stress, which was fabricated without damage.

Structures I0H0, I0H2, I4H0, and I8H0, which did not show bistable characteristics in the FEM analysis, deformed in the opposite direction to

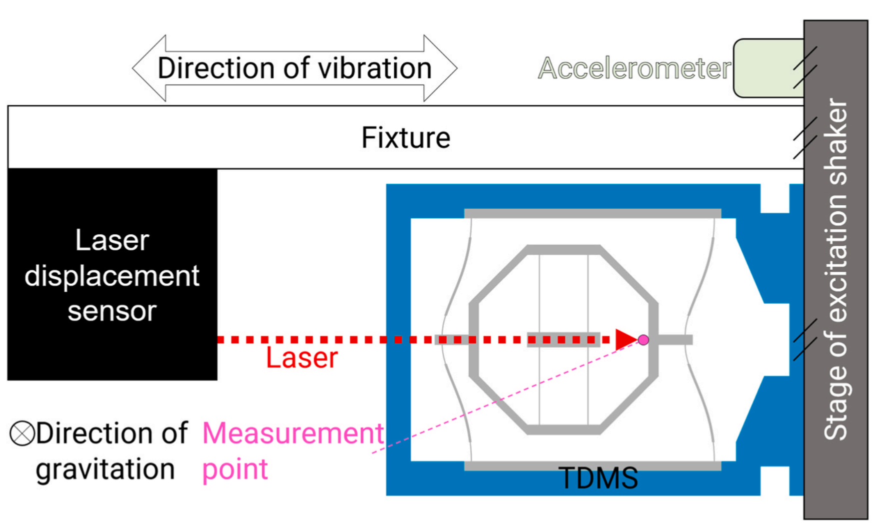

Fig. 6. Schematic image of vibration experiment system.

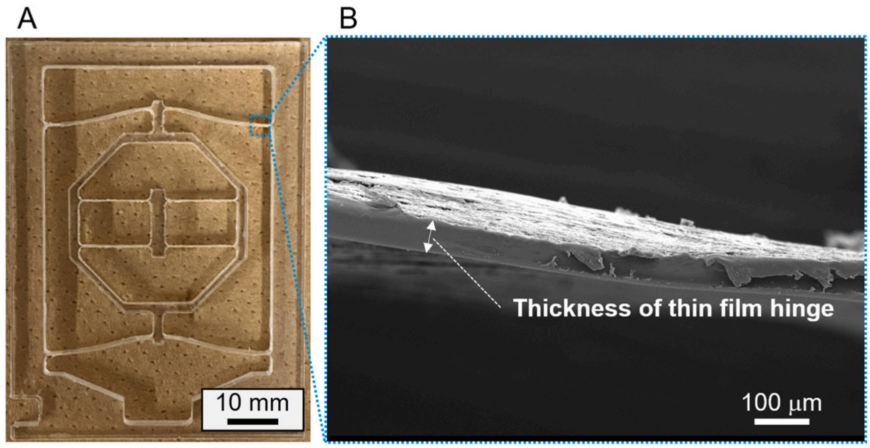

Fig. 7. Fabricated TDMS. (A) Photograph of fabricated TDMS. (B) SEM image of thin film hinge of TDMS.

the original curve when a force was applied. However, when the force was removed, the beam returned to its initial orientation. This indicated that these structures had only one stable position and were monostable. Therefore, as shown in the FEM analysis results, structures I0H0, I0H2, I4H0, and I8H0 were not bistable. However, all the other structures that were shown to be bistable by the FEM analysis deformed in the opposite direction of the curve when force was applied and did not return to the original stable position even after the force was removed. This indicates that these structures have two stable positions and are bistable. Therefore, stable and bistable structures can be fabricated without internal stress by cutting them in one direction.

The TDMS, which includes a structure that mimics the FCI, was fabricated by milling in one direction using an NC milling machine. This demonstrates that the structure of the FCI is two-dimensional, and similar structures can be easily fabricated using semiconductor/MEMS processing techniques, such as photolithography, that perform machining on a two-dimensional plane. MEMS VEHs are advantageous in miniaturization and mass production as they are fabricated using semiconductor/MEMS processing techniques that are an advantage in miniaturization and mass production. However, the bistable structure proposed in previous research, which has a buckling beam with a magnet and internal stress, involves many processes that are not used in general semiconductor/MEMS processing techniques, such as aligning magnetic materials and adding deformations. This makes it difficult to complete fabrication within normal semiconductor/MEMS fabrication processes, making it difficult to combine with the semiconductor/MEMS processing techniques of MEMS VEHs. On the other hand, the proposed FCI can be fabricated on a two-dimensional plane and does not require the assembly of magnetic materials or the addition of deformations after fabrication; therefore, it is expected that FCI can be fabricated and assembled with MEMS VEHs in the same manufacturing line.

5.2. Vibrational experiment

Three measurement values “the maximum vibrational acceleration amplitude inputted using feedback control from an accelerometer on the excitation stage,” “the calculated average acceleration derived from the maximum acceleration amplitude,” and “the measured average acceleration calculated by differentiating the displacement of the excitation stage measured with a laser displacement meter using the second derivative with the central difference method” were compared. The calculated average acceleration is approximately 63.7 % of the maximum vibrational acceleration amplitude. The calculated average acceleration, measured average acceleration, and their ratios for each maximum vibrational acceleration amplitude are shown in Fig. 8. The x-axis represents the maximum vibrational acceleration amplitude set by the vibrator, which was varied at intervals of 2.5 m/s^2 from 1 m/s^2 to

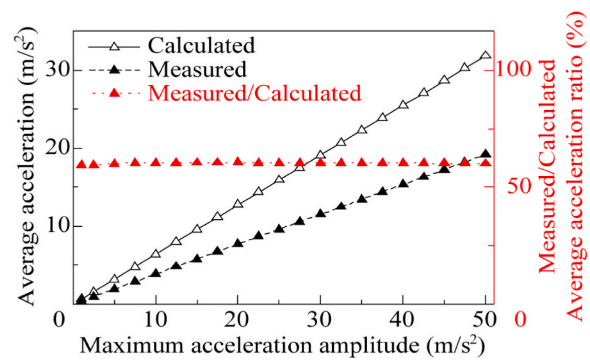

Fig. 8. Calculated and measured average acceleration and ratio of these value. Unfilled triangle indicates calculated average acceleration. Filled triangle indicates measured acceleration. Red triangle indicates the ratio of calculated and measured average acceleration.

50 m/s^2. The y axis represents the calculated and measured average accelerations. The r-axis represents the ratio obtained by dividing the measured average acceleration by the calculated average acceleration. Under all conditions of maximum vibrational acceleration amplitude, the measured average acceleration was smaller than the calculated average acceleration. The minimum and maximum values of the ratio of the measured average acceleration to the calculated average acceleration for each maximum vibrational acceleration amplitude were 59.39 % and 60.55 %, respectively. The mean and standard deviation were 60.24 % ± 0.28 %. The difference between the maximum and minimum values of the ratio of the measured average acceleration to the calculated average acceleration was 1.16 %, which was almost constant. The average acceleration measured with a laser displacement meter was approximately 60.24 % of the arithmetic average acceleration, which was thought to be due to errors during the displacement measurement and errors caused by the differentiation interval. Because these errors occurred at a constant rate, regardless of the magnitude of the original vibration acceleration, the measurement method was found to be reproducible. Therefore, by differentiating the displacement acquired by the laser displacement meter using the second derivative with the central difference method, the acceleration applied from the excitation stage to the TDMS and the output acceleration generated by the primary beam of the TDMS were directly compared using the average acceleration derived from the second derivative using the central difference method.

An experimental system for measuring the displacement of the primary beam of the TDMS was developed by setting up the fabricated TDMS and a laser displacement sensor. The TDMS setup of the experimental vibration system is shown in Fig. 9. The vibration direction is set perpendicular to the direction of gravity. The vibration of the solid part when a 10 Hz vibration was applied to the I4H4 structure, which was suggested to have bistable characteristics from the FEM analysis, was measured by the laser displacement sensor. The measured vibration waveforms and FFT results are shown in Fig. 10. When ST occurred, the direction of the no-internal stress curved-beam was reversed, so a large displacement of more than ± 1 mm was observed. When the average acceleration is set to 0.18 m/s^2, the I4H4 model vibrates without an accompanying ST (Fig. 10 (A)). In the FFT results, a clear peak was observed at an applied frequency of 10 Hz (Fig. 10 (D)). When the average acceleration was set to 0.35 m/s^2, ST was observed where the bending direction of the no-internal stress curved-beam was reversed, and the measured amplitude was a large displacement compared to the applied acceleration of 10 m/s^2 (Fig. 10 (B)). In the FFT results, a peak was observed at an applied frequency of 10 Hz, and the vibration frequency was more dispersed than the other vibrations (Fig. 10 (E)). Even when the average acceleration was set to 0.51 m/s^2, the ST was observed (Fig. 10 (C)). In the FFT results, a clear peak was observed at an applied frequency of 10 Hz (Fig. 10 (F)). Similar vibration waveforms were observed in other models that exhibited N-shaped F-D curves. From the vibration waveforms, the TDMS with N-shaped F-D curves exhibited intrawell oscillations, chaotic vibrations, and interwell oscillations, which are characteristic of bistable structures. Therefore, the FCI fabricated by unidirectional milling can produce large displacements owing to the ST as a bistable structure and can convert applied vibrations.

The output acceleration of the solid part of the TDMS was calculated when a constant acceleration was applied. To evaluate the effect of the vibration of the oscillatory structure of the MEMS VEH, the acceleration of the solid part measured when the mass was vibrated is shown in Fig. 11(A), and the acceleration of the solid part measured when the mass was not vibrated is shown in Fig. 11(B). The model in which the mass part is vibrated is denoted by (_V) at the end of each structure name, and the model in which the mass part is not vibrated is denoted by (_N). When the mass vibrated, an output acceleration larger than the applied acceleration was measured under certain conditions. However, when the mass part did not vibrate, no output acceleration larger than the applied acceleration was measured. In addition, the ST was observed under 11 conditions. The applied and output accelerations at the ST are shown in Fig. 11 (C). For samples with the same design, ST occurred at a smaller applied acceleration when the mass part was vibrated. For each

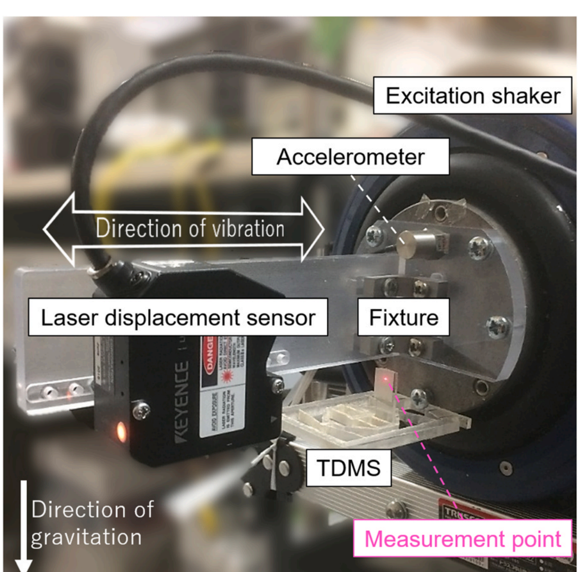

Fig. 9. Photograph of vibration experiment system.

TDMS design, a graph showing the difference in applied acceleration that caused ST when the mass part was vibrated and when it was not vibrated on the horizontal axis and the ratio of applied acceleration to output acceleration at the ST on the vertical axis are shown in Fig. 11(D). In Fig. 11(D), the designs in the right direction of the graph cause ST to have a smaller applied acceleration when the mass is vibrated compared to when the mass is not vibrated. The conditions in the vertical direction of the graph indicate that vibrations can be converted with high efficiency. The I4H2 and I8H2 models cause ST at the same applied acceleration, regardless of the vibration of the mass. In the other models, the difference in the applied acceleration at the ST was largest in the order of I0H2, I8H4, and I4H4. The output acceleration when ST occurred was larger when the mass part vibrated under all conditions. In addition, the conditions under which the output acceleration was greater than the applied acceleration were I4H2_V, I8H2_V, and I8H4_V, all of which were conditions in which the mass vibrated. When the mass part, which mimics the oscillatory structure of the MEMS VEH, vibrates, it always causes ST at a smaller applied acceleration and generates a larger output acceleration compared to the condition in which the mass part is not vibrated. Furthermore, under the three conditions, I4H2_V, I8H2_V, and I8H4_V, an output acceleration larger than the applied acceleration was generated. In particular, under the condition of I4H2_V, an output acceleration of more than 1.3 times the applied acceleration was measured. The output acceleration was larger under all five conditions, as shown in Fig. 11(D), where the oscillator vibrated. It is expected that ST was induced by the temporary resonance of the vibration of the mass and the no-internal stress curved-beam. Because the induction of ST by temporary resonance is thought to occur even in the FCI and MEMS VEH with an oscillatory structure, the vibration energy in the environment can be recovered with extremely high efficiency by assembling the FCI with a bistable structure and the MEMS VEH with an oscillatory structure. Therefore, it is expected that by simply assembling an MEMS VEH with an oscillatory structure on an FCI with a bistable structure, a large acceleration at the ST can be applied to the MEMS VEH regardless of the frequency of vibration in the environment.

The analysis did not show a clear correlation between the symmetry of the F-D curve of each model and the ease of ST occurrence or output acceleration in the vibration experiment. For the initial displacement type of the primary beam, the energy required to move from the first stable equilibrium point, which is the initial state, to the second stable equilibrium point is always greater than the energy required to return from the second stable equilibrium point to the first stable equilibrium point. In this experimental system, where the same magnitude of acceleration is applied bidirectionally to a bistable structure, the condition that applies the acceleration necessary to move from the first to the second stable equilibrium point inevitably causes movement from the second to the first stable equilibrium point. Hence, no relationship was observed between the symmetry of the F-D curve and the occurrence of ST or output acceleration. However, in environments where the magnitude of the input acceleration differs depending on the direction, such as walking vibrations, or where the influence of gravity is present, adjusting the point symmetry of the F-D curve can produce ST more stably and efficiently in each environment [39–41].

I0H2 forms an N-shaped F-D curve but does not exhibit a negative f_{bot}, indicating that it is not a bistable structure. However, similar to other bistable TDMS, ST occurs efficiently when a mass is vibrated. Even without a second stable equilibrium point, shapes that exhibit an N-shaped F-D curve can cause significant displacement and efficiently harvest vibrational energy from the environment. Because I0H2 lacks a thin film hinge, incorporating shapes without thin film hinges into the FCI could be advantageous for applications requiring high applied accelerations or long-term durability, as they are less prone to stress concentration during deformation. However, all shapes that produced an output acceleration greater than the input acceleration in the experiments were bistable structures with a negative f_{bot}. Therefore, to harvest environmental vibrations efficiently, it is appropriate to

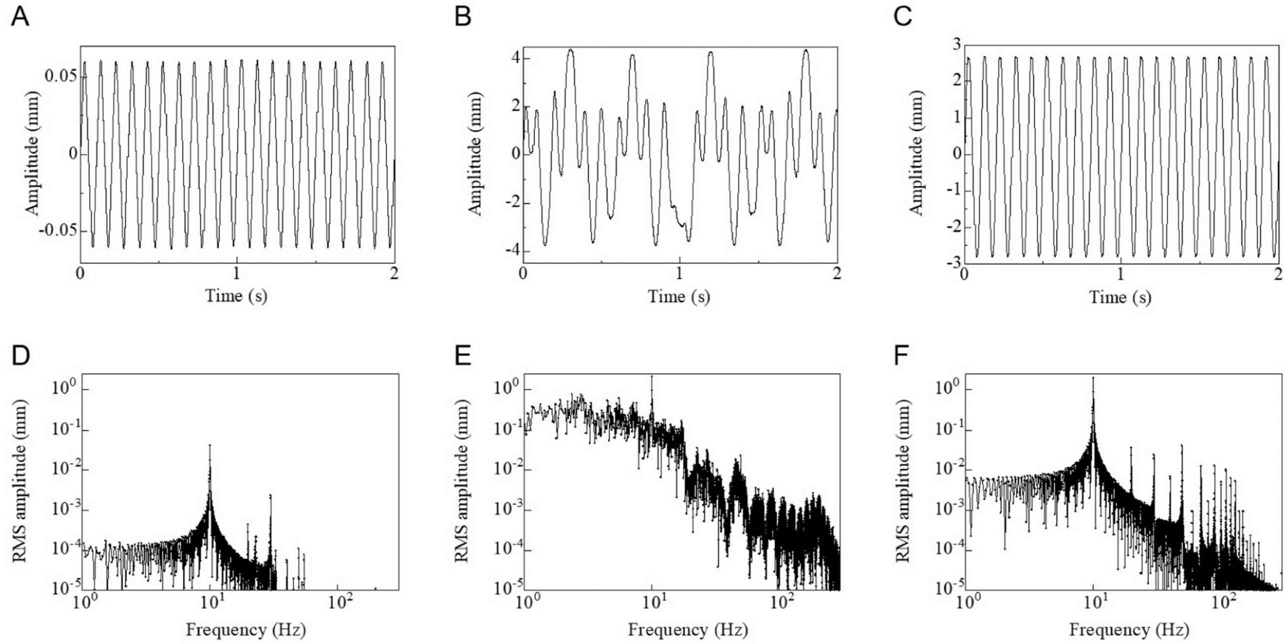

Fig. 10. Amplitude-time responses (top row) and fast fourier transformed plot (bottom row) of I4H4 model. (A)(D) Applied acceleration is 10 m/s^2 (Intrawell oscillations). (B)(E) Applied acceleration is 20 m/s^2 (Chaotic vibrations). (C)(F) Applied acceleration is 30 m/s^2 (Interwell oscillations).

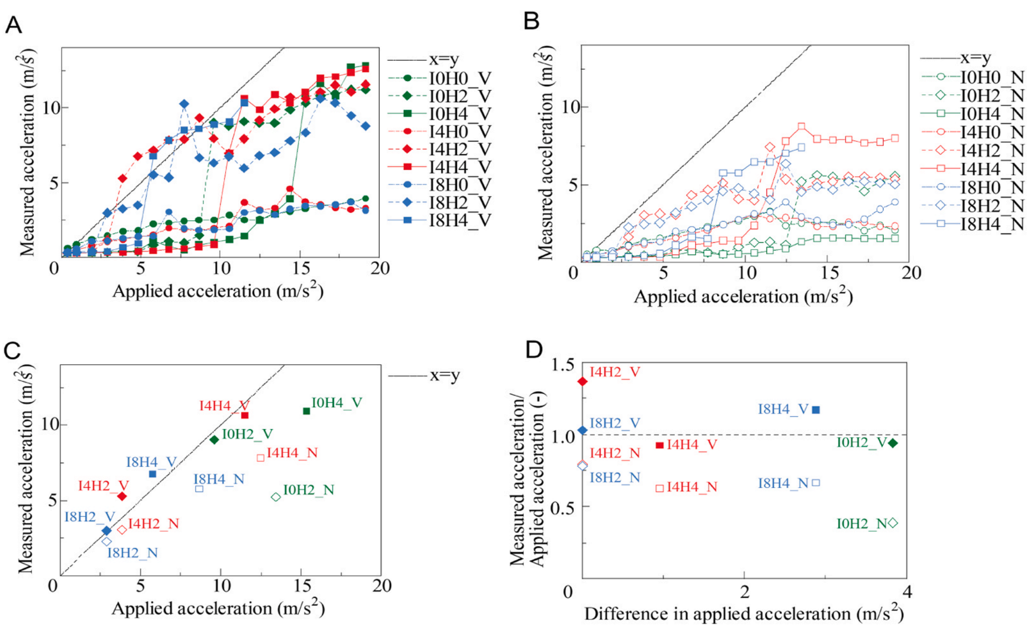

Fig. 11. Measured acceleration of solid part of TDMSs. (A) Measured acceleration of solid part of TDMSs with mass part vibration. (B) Measured acceleration of solid part of TDMSs without mass part vibration. (C) Measured acceleration of ST points. (D) Measured/Applied acceleration difference in applied acceleration between same design TDMSs.

incorporate bistable structures into FCI.

The bistable structure undergoes a large displacement and vibrates with a large acceleration at ST. ST is generated by releasing the potential energy of the bistable structure, that is, a no-internal stress curved-beam, when the force determined by the acceleration of the applied vibrations and the mass of the oscillatory structure cause the no-internal stress curved-beam to deform over d_{mid}. Because ST can occur regardless of the applied vibration frequency, the FCI can convert the energy of random environmental vibrations into ST vibrations by applying the acceleration generated by the ST to the MEMS VEH. Furthermore, by designing these parameters, such as the thin film hinge length of the no-internal stress curved-beam, to consider only the acceleration of vibrations expected to occur in the operating environment of the MEMS VEH, high efficiency power generation accompanied by ST is expected because the minimum acceleration required to induce ST is determined by the initial displacement of the no-internal stress curved-beam and the length of the thin film hinge. Additionally, the oscillatory structure of the MEMS VEH induces ST, and an output acceleration of more than 1.3 times the applied acceleration was detected at the ST in this study. When the oscillatory structure of the MEMS VEH undergoes sinusoidal or decaying sinusoidal vibrations, power generation is normally proportional to the square of the input acceleration. However, the vibrations caused by the FCI are nonlinear and not sinusoidal. Thus, the vibrator of the MEMS VEH does not always produce sinusoidal or decaying sinusoidal vibrations when subjected to nonlinear acceleration. Therefore, the power generation of a MEMS VEH is not always proportional to the square of the applied acceleration. However, even when nonlinear vibrations are applied, the oscillatory structure of a non-bistable MEMS VEH generates sinusoidal vibrations; thus, the power generation of the MEMS VEH is expected to increase approximately quadratically with an increase in the applied acceleration. Thus, the proposed FCI can improve the power generation efficiency of the MEMS VEH by approximately 1.69 times [26]. Consequently, a power generation device combining FCI and MEMS VEH is expected to be a highly efficient power source for sensor nodes.

6. Conclusions

To improve the power generation efficiency of the MEMS VEH, we evaluated the usefulness of the FCI, which has a bistable no-internal stress curved-beam, through vibration experiments using the TDMS, which has a structure that simulates the oscillatory structure of the MEMS VEH and FCI. TDMS is a planar, bistable structure that does not require any internal stress or assembly for the addition of magnetic materials at the time of manufacture, indicating that FCI can easily be miniaturized and mass-produced by two-dimensional planar processing, which is a semiconductor/MEMS processing technology, and can be assembled with an MEMS VEH. Through FEM analysis and vibration experiments using TDMS, it was indicated that the ST by the no-internal stress curved-beam of FCI, which produces an acceleration that does not correlate with the vibration mode or frequency of vibration in the environment, is induced by the oscillatory structure of the MEMS VEH. In addition, it was also indicated that an output acceleration of more than 1.3 times the maximum acceleration of vibration in the environment is supplied from the FCI to the MEMS VEH at ST. Because the generated power of the MEMS VEH is proportional to the square of the applied acceleration, the generated power of the MEMS VEH can be improved by more than 1.69 times by FCI. Furthermore, the FCI can easily optimize the required applied acceleration that causes ST to the applied acceleration expected in an environment where the MEMS VEH is used, only by changing the initial displacement of its no-internal stress curved-beam and the length of the thin film hinge. Therefore, the FCI is useful for improving the power generation efficiency of MEMS VEH in various environments.

7. CRediT authorship contribution statement

Hiroshi Toshiyoshi: Writing – review & editing, Supervision, Project administration, Methodology, Funding acquisition, Conceptualization. **Takaaki Suzuki:** Writing – review & editing, Writing – original draft, Supervision, Project administration, Methodology, Funding acquisition, Conceptualization. **Hidetaka Ueno:** Writing – review & editing, Writing – original draft, Validation, Project administration, Methodology, Investigation, Funding acquisition, Conceptualization.

Declaration of Competing Interest

The authors report no declarations of interest.

Data Availability

Data will be made available on request.

Acknowledgements

This research was partially supported by JST CREST Grant Number JPMJCR19Q2, JSPS KAKENHI Grant Numbers JP22K14583, JP23H01363, and the Gunma University Priority Support Project R04-01.

References

[1] S. Madakam, R. Ramaswamy, S. Tripathi, Internet of things (IoT): a literature review, JCC 03 (2015) 164–173, https://doi.org/10.4236/jcc.2015.35021.
[2] S. Zhang, H. Zhang, A review of wireless sensor networks and its applications, in: 2012 IEEE International Conference on Automation and Logistics, IEEE, Zhengzhou, China, 2012: pp. 386–389. https://doi.org/10.1109/ICAL.2012.6308240.
[3] M. Sowmya, K. Srinivas, Literature survey on wireless sensor networks, Int. J. Eng. Res. (3) (2014) (https://www.ijert.org/literature-survey-on-wireless-sensor-networks).
[4] S. Kaminaga, , Trillion sensors and MEMS, Sens. Mater. (2018) 723, https://doi.org/10.18494/SAM.2018.1814.
[5] F.K. Shaikh, S. Zeadally, Energy harvesting in wireless sensor networks: a comprehensive review, Renew. Sustain. Energy Rev. 55 (2016) 1041–1054, https://doi.org/10.1016/j.rser.2015.11.010.
[6] A. Hande, T. Polk, W. Walker, D. Bhatia, Indoor solar energy harvesting for sensor network router nodes, Microprocess. Microsyst. 31 (2007) 420–432, https://doi.org/10.1016/j.micpro.2007.02.006.
[7] A. Cuadras, M. Gasulla, V. Ferrari, Thermal energy harvesting through pyroelectricity, Sens. Actuators A Phys. 158 (2010) 132–139, https://doi.org/10.1016/j.sna.2009.12.018.
[8] T.S. Almoneef, F. Erkmen, O.M. Ramahi, Harvesting the energy of multi-polarized electromagnetic waves, Sci. Rep. 7 (2017) 14656, https://doi.org/10.1038/s41598-017-15298-5.
[9] C. Wei, X. Jing, A comprehensive review on vibration energy harvesting: modelling and realization, Renew. Sustain. Energy Rev. 74 (2017) 1–18, https://doi.org/10.1016/j.rser.2017.01.073.
[10] S. Roundy, P.K. Wright, J. Rabaey, A study of low level vibrations as a power source for wireless sensor nodes, Comput. Commun. 26 (2003) 1131–1144, https://doi.org/10.1016/S0140-3664(02)00248-7.
[11] C. Dagdeviren, P. Joe, O.L. Tuzman, K.-I. Park, K.J. Lee, Y. Shi, Y. Huang, J. A. Rogers, Recent progress in flexible and stretchable piezoelectric devices for mechanical energy harvesting, sensing and actuation, Extrem. Mech. Lett. 9 (2016) 269–281, https://doi.org/10.1016/j.eml.2016.05.015.
[12] X. Ma, S. Zhou, A review of flow-induced vibration energy harvesters, Energy Convers. Manag. 254 (2022) 115223, https://doi.org/10.1016/j.enconman.2022.115223.
[13] W. Zhou, G.R. Penamalli, L. Zuo, An efficient vibration energy harvester with a multi-mode dynamic magnifier, Smart Mater. Struct. 21 (2012) 015014, https://doi.org/10.1088/0964-1726/21/1/015014.
[14] H.S. Kim, J.-H. Kim, J. Kim, A review of piezoelectric energy harvesting based on vibration, Int. J. Precis. Eng. Manuf. 12 (2011) 1129–1141, https://doi.org/10.1007/s12541-011-0151-3.
[15] B. Yang, C. Lee, W. Xiang, J. Xie, J. Han He, R.K. Kotlanka, S.P. Low, H. Feng, Electromagnetic energy harvesting from vibrations of multiple frequencies, J. Micromech. Microeng. 19 (2009) 035001, https://doi.org/10.1088/0960-1317/19/3/035001.
[16] L.-C. Zhao, H.-X. Zou, Q.-H. Gao, G. Yan, F.-R. Liu, T. Tan, K.-X. Wei, W.-M. Zhang, Magnetically modulated orbit for human motion energy harvesting, Appl. Phys. Lett. 115 (2019) 263902, https://doi.org/10.1063/1.5131193.
[17] Y. Zi, H. Guo, Z. Wen, M.-H. Yeh, C. Hu, Z.L. Wang, Harvesting low-frequency (<5 Hz) irregular mechanical energy: a possible killer application of triboelectric nanogenerator, ACS Nano 10 (2016) 4797–4805, https://doi.org/10.1021/acsnano.6b01569.
[18] Y. Suzuki, Electret based vibration energy harvester for sensor network, in: 2015 Transducers - 2015 18th International Conference on Solid-State Sensors, Actuators and Microsystems (TRANSDUCERS), IEEE, Anchorage, AK, USA, 2015: pp. 43–46. https://doi.org/10.1109/TRANSDUCERS.2015.7180856.
[19] M.M. Ahmad, F.U. Khan, Review of vibration-based electromagnetic–piezoelectric hybrid energy harvesters, Int. J. Energy Res. 45 (2021) 5058–5097, https://doi.org/10.1002/er.6253.
[20] M. Zhu, Q. Shi, T. He, Z. Yi, Y. Ma, B. Yang, T. Chen, C. Lee, Self-powered and self-functional cotton sock using piezoelectric and triboelectric hybrid mechanism for healthcare and sports monitoring, ACS Nano (2019) acsnano.8b08329, https://doi.org/10.1021/acsnano.8b08329.
[21] J.-Q. Liu, H.-B. Fang, Z.-Y. Xu, X.-H. Mao, X.-C. Shen, D. Chen, H. Liao, B.-C. Cai, A MEMS-based piezoelectric power generator array for vibration energy harvesting, Microelectron. J. 39 (2008) 802–806, https://doi.org/10.1016/j.mejo.2007.12.017.
[22] W.J. Choi, Y. Jeon, J.-H. Jeong, R. Sood, S.G. Kim, Energy harvesting MEMS device based on thin film piezoelectric cantilevers, J. Electroceram 17 (2006) 543–548, https://doi.org/10.1007/s10832-006-6287-3.
[23] H. Honma, H. Mitsuya, G. Hashiguchi, H. Fujita, H. Toshiyoshi, Improvement of energy conversion effectiveness and maximum output power of electrostatic induction-type MEMS energy harvesters by using symmetric comb-electrode structures, J. Micromech. Microeng. 28 (2018) 064005, https://doi.org/10.1088/1361-6439/aab514.
[24] T. Tsukamoto, Y. Umino, S. Shiomi, K. Yamada, T. Suzuki, Bimorph piezoelectric vibration energy harvester with flexible 3D meshed-core structure for low frequency vibration, Sci. Technol. Adv. Mater. 19 (2018) 660–668, https://doi.org/10.1080/14686996.2018.1508985.
[25] R. Ichige, N. Kuriyama, Y. Umino, T. Tsukamoto, T. Suzuki, Size optimization of metamaterial structure for elastic layer of a piezoelectric vibration energy harvester, Sens. Actuators A: Phys. 318 (2021) 112488, https://doi.org/10.1016/j.sna.2020.112488.

[26] H. Toshiyoshi, S. Ju, H. Honma, C.-H. Ji, H. Fujita, MEMS vibrational energy harvesters, Sci. Technol. Adv. Mater. 20 (2019) 124–143, https://doi.org/10.1080/14686996.2019.1569828.
[27] R.L. Harne, K.W. Wang, A review of the recent research on vibration energy harvesting via bistable systems, Smart Mater. Struct. 22 (2013) 023001, https://doi.org/10.1088/0964-1726/22/2/023001.
[28] B. Camescasse, A. Fernandes, J. Pouget, Bistable buckled beam and force actuation: experimental validations, Int. J. Solids Struct. 51 (2014) 1750–1757, https://doi.org/10.1016/j.ijsolstr.2014.01.017.
[29] S.P. Pellegrini, N. Tolou, M. Schenk, J.L. Herder, Bistable vibration energy harvesters: a review, J. Intell. Mater. Syst. Struct. 24 (2013) 1303–1312, https://doi.org/10.1177/1045389X12444940.
[30] A. Cammarano, S.G. Burrow, D.A.W. Barton, Modelling and experimental characterization of an energy harvester with bi-stable compliance characteristics, Proc. Inst. Mech. Eng. Part I J. Syst. Control Eng. 225 (2011) 475–484, https://doi.org/10.1177/0959651811403093.
[31] A. Morel, L. Charleux, Q. Demouron, A. Benhemou, D. Gibus, C. Saint-Martin, A. Carré, É. Roux, T. Huguet, A. Badel, Simple analytical models and analysis of bistable vibration energy harvesters, Smart Mater. Struct. 31 (2022) 105016, https://doi.org/10.1088/1361-665X/ac8d3d.
[32] J. Qiu, J.H. Lang, A.H. Slocum, A centrally-clamped parallel-beam bistable MEMS mechanism, in: Technical Digest. MEMS 2001. 14th IEEE International Conference on Micro Electro Mechanical Systems (Cat. No.01CH37090), IEEE, Interlaken, Switzerland, 2001: pp. 353–356. https://doi.org/10.1109/MEMSYS.2001.906551.
[33] J. Qiu, J.H. Lang, A.H. Slocum, A curved-beam bistable mechanism, J. Micro Syst. 13 (2004) 137–146, https://doi.org/10.1109/JMEMS.2004.825308.
[34] D.-A. Wang, H.-T. Pham, Y.-H. Hsieh, Dynamical switching of an electromagnetically driven compliant bistable mechanism, Sens. Actuators A Phys. 149 (2009) 143–151, https://doi.org/10.1016/j.sna.2008.11.004.
[35] S. Park, D. Hah, Pre-shaped buckled-beam actuators: theory and experiments, Sens. Actuators A: Phys. 148 (2008) 186–192, https://doi.org/10.1016/j.sna.2008.07.009.
[36] A. El Amrani, A. Benali, M. Bouya, M. Faqir, K. Demir, A. Hadjoudja, M. Ghogho, A study of through package vias in a glass interposer for multifunctional and miniaturized systems, Microelectron. Reliab. 54 (2014) 1972–1976, https://doi.org/10.1016/j.microrel.2014.07.108.
[37] K.A. Cook-Chennault, N. Thambi, A.M. Sastry, Powering MEMS portable devices—a review of non-regenerative and regenerative power supply systems with special emphasis on piezoelectric energy harvesting systems, Smart Mater. Struct. 17 (2008) 043001, https://doi.org/10.1088/0964-1726/17/4/043001.
[38] S.-S. Yoon, S.-H. Lee, G.-C. Hwang, M.-K. Choi, B.-G. Kang, H. Kim, K.-S. Jang, Mechanical, thermal, and rheological properties of phlogopite-incorporated polycarbonate and polystyrene, Macromol. Res. 30 (2022) 365–374, https://doi.org/10.1007/s13233-022-0045-5.
[39] K. Yamamoto, T. Fujita, A. Badel, K. Kanda, K. Maenaka, Design and fabrication of parallel curved spring for nonlinear energy harvester, Procedia Eng. 120 (2015) 651–654, https://doi.org/10.1016/j.proeng.2015.08.697.
[40] K. Yamamoto, A. Badel, F. Formosa, L. Charleux, T. Fujita, K. Kanda, K. Maenaka, Non-linear vibration electret-harvester with optimized curved beam for low-frequency operation, J. Phys.: Conf. Ser. 1052 (2018) 012122, https://doi.org/10.1088/1742-6596/1052/1/012122.
[41] K. Yamamoto, T. Fujita, A. Badel, F. Formosa, K. Kanda, K. Maenaka, Vibration energy harvester with Bi-stable curved beam spring offset by gravitational acceleration, J. Phys. Conf. Ser. 660 (2015) 012127, https://doi.org/10.1088/1742-6596/660/1/012127.

Hidetaka Ueno received his B.S. and M.S. degrees from Kagawa University, Japan, in 2014 and 2016, respectively. He received his Ph.D. degree from Gunma University, Japan, in 2019. From 2019–2020, he was a postdoctoral researcher at Gunma University. From 2020–2023, he was a postdoctoral researcher at the National Institute of Advanced Industrial Science and Technology. Since 2023, he has been a project assistant professor at Kobe University. His research field is bioengineering. (hueno@people.kobe-u.ac.jp).

Hiroshi Toshiyoshi received his M.E. and Ph.D. degrees in electrical engineering from The University of Tokyo, Tokyo, Japan, in 1993 and 1996, respectively. He joined the Institute of Industrial Science (IIS), The University of Tokyo, in 1996 as a lecturer. From 1999–2001, he was a visiting assistant professor at the University of California, Los Angeles, CA, U.S.A. In 2002, he became an associate professor with the IIS, The University of Tokyo. From 2005–2008, he was the project leader of the Optomechatronics Project at the Kanagawa Academy of Science and Technology, Kawasaki, Japan. Since 2009, he has been a professor with the IIS, The University of Tokyo. His research interests include optical and power MEMS. (hiro@iis.u-tokyo.ac.jp).

Takaaki Suzuki received his B.E. and M.E. degrees from Gunma University, Japan, in 1998 and 2000, respectively. He also received his Ph.D. degree from Kyoto University, Japan, in 2003. From 2004–2008, he was an assistant professor at Kyoto University. From 2008–2015, he was an associate professor at Kagawa University. From 2015–2018, he was an associate professor at Gunma University. Since 2018, he has been a professor at the Division of Mechanical Science & Technology, Gunma University. From 2015–2019, he was also a PRESTO researcher at the Japan Science and Technology Agency. His research interests include the development of novel microfabrication technology, microfluidic systems for gene and cell analyses, and an energy harvester for IoT. He is a member of IEEE, the Japan Society of Mechanical Engineers, the Institute of Electrical Engineers of Japan, and so forth. (suzuki.taka@gunma-u.ac.jp).